Engineering boundary-dominated topological states in defective hyperbolic lattices

Qingsong Pei, Hao Yuan, Weixuan Zhang,[*] and Xiangdong Zhang

Key Laboratory of Advanced Optoelectronic Quantum Architecture and Measurements of Ministry of Education, Beijing Key Laboratory of Nanophotonics & Ultrafine Optoelectronic Systems, School of Physics, Beijing Institute of Technology, 100081, Beijing, China

Topological matters with lattice disclinations have been widely investigated in Euclidean space. In recent years, exotic topological phases in hyperbolic lattices, which are regular tessellations in the curved space with a constant negative curvature, have been theoretically proposed and experimentally observed, while the investigation of topologically defective hyperbolic lattices is still lacking. Here, we study topological states in the hyperbolic lattice with polygonal defects. It is shown that the topologically one-way boundary state can still exist in the defective hyperbolic Haldane model. Interestingly, we find that only a single bulk site can induce the formation of boundary-dominated one-way propagations in defective hyperbolic lattices. In experiments, we fabricate the defective hyperbolic circuit with a single bulk site to detect the boundary-dominated topological state. Frequency-dependent impedance responses clearly illustrate the existence of nontrivial band gaps and midgap topological boundary states. Furthermore, the backscattering-immune propagation protected by a single bulk site is observed by measuring the dynamics of voltage packet. Our work suggests a useful platform to study topological phases in defective hyperbolic lattices, and may have potential applications in designing high-efficient topological devices with an extremely small bulk region.

I. INTRODUCTION

Defects always exist in natural and artificial materials. Many investigations have shown that topological defects can play the unique role in various topological matters, where topological modes can occur on bulk defects in topological materials [1–6]. Motivated by previous theoretical predictions, experimental realizations of nontrivial topological defect modes both in condensed-matter systems and classical wave platforms are reported. For example, the zero-dimensional topological modes are found at dislocations [7–9] and disclinations [10,11] in topological crystalline insulators. The one-dimensional helical modes are localized at dislocations in weak topological insulators [12–14]. Beyond Hermitian systems, the non-Hermitian skin effects can also be induced by topological defects [15–18]. To date, all of the established topological states in defective systems mainly focus on Euclidean geometry with a zero curvature.

On the other hand, the non-Euclidean geometry widely exists in nature and plays important roles in various areas. Hyperbolic lattices, which are regular tessellations in the curved space with a constant negative curvature, have been investigated as mathematical objects over past decades [19]. Recently, using circuit quantum electrodynamics [20] and electric circuits [21], the experimental realization of discrete hyperbolic lattices has stimulated many advances in non-Euclidean geometry and hyperbolic physics, including hyperbolic band theory [22,23], the crystallography of hyperbolic lattices [24], quantum-field theories in continuous negatively curved spaces [25], hyperbolic flatbands [26], Bloch bands of hyperbolic graphene [27], and so on [28–32]. Beyond these hyperbolic physical phenomena, there are many investigations on the construction of hyperbolic topological states [33–38]. For example, the hyperbolic quantum spin Hall effect was theoretically proposed based on a treelike design of the Landau gauge in periodic and open systems [33,34]. Hyperbolic Chern insulators have been theoretically proposed and experimentally fulfilled by circuit networks [35–37]. One of the most important advances of hyperbolic topological states is the boundary-dominated spatial profile, which results from the finite ratio between the number of boundary sites to that of total sites in the thermodynamic limit. Motivated by currently proposed boundary-dominated topological states on defect-free hyperbolic lattices, it is interesting to ask do topological boundary states exist in defective hyperbolic lattices? And, could we further increase the ratio of boundary sites in defective hyperbolic lattices to create one-way topological states with much fewer bulk sites than that of defect-free hyperbolic counterparts?

In this work, we report the realization of backscattering-immune topological states in the hyperbolic lattice with polygonal defects. It is found that the boundary-dominated one-way topological states exist in the defective hyperbolic Haldane model. As for the defective hyperbolic Haldane model without any bulk sites, the robust boundary propagation disappears owing to the fact that all lattice sites belong to the boundary passageway. In this case, there is no way to bypass the boundary obstacle, making the significant backscattering appear. Interestingly, we find that by adding a single bulk site, the backscattering-immune topological states can reappear in the defective hyperbolic Haldane model. Such a defective hyperbolic lattice-inspired topological state may be used to

---

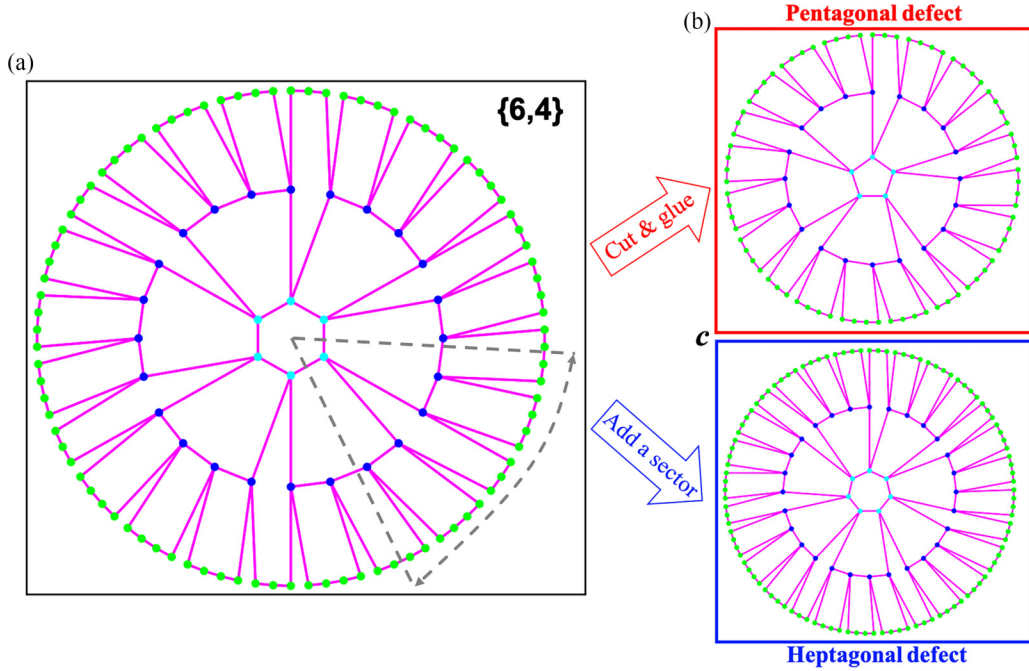[*]Author to whom any correspondence should be addressed: zhangwx@bit.edu.cn

FIG. 1. Schematic diagram for the {6,4} hyperbolic lattice with a central defect. (a) Finite hyperbolic lattice {6,4} in the form of successive quasiconcentric rings with $L = 3$ layers. Hyperbolic lattice sites in the first, second, and third layers are marked by cyan, blue, and green dots, respectively. (b) The {6,4} hyperbolic lattice with a central pentagonal defect can be constructed by removing a $\pi/3$ sector (enclosed by a dashed block) of the perfect {6,4} hyperbolic lattice and gluing two cutting boundaries together. (c) The {6,4} hyperbolic lattice with a central heptagonal defect can be constructed by adding a $\pi/3$ sector to the perfect {6,4} hyperbolic lattice.

design high-efficient topological devices with an extremely narrow bulk region. In experiments, we fabricate a defective hyperbolic circuit to detect the boundary-dominated topological state. The measurements of impedance and voltage dynamics clearly demonstrate the realization of one-way topological states protected by a single bulk site.

II. ENGINEERING BOUNDARY-DOMINATED ONE-WAY TOPOLOGICAL STATES IN DEFECTIVE HYPERBOLIC LATTICES

We consider the hexagonal hyperbolic lattice embedded into the Poincaré disk. The hyperbolic lattice is labeled by the Schläfli notation of {6,4}, manifesting the tessellation of a plane by 6-sided regular polygons with the coordination number being 4. It is noted that the Hamiltonian of {6,4} hyperbolic tight-binding lattice model is only depending on the connection pattern of different sites. In this case, the {6,4} hyperbolic lattice could be illustrated by arranging all vertices in the form of quasiconcentric rings. Figure 1(a) presents the three-layer concentric-ring counterpart of the finite {6,4} hyperbolic lattice, where lattice sites in the first, second, and third layers are represented by cyan, blue, and green dots, respectively. By deleting a $\pi/3$ sector (enclosed by the dashed block) and reattaching the seams, a central pentagonal defect is generated, as shown in Fig. 1(b). Similarly, inserting such a $\pi/3$ sector into the original {6,4} hyperbolic lattices, a central heptagonal appears, as shown in Fig. 1(c). Such a method can be used to generate hyperbolic lattices possessing a central bulk defect with arbitrary N-sided regular polygon.

To construct topological states in the defective {6,4} hyperbolic lattice, we extend the Haldane model to this structure. In particular, we introduce the real-valued nearest-neighbor hopping (t_1) and the complex-valued next-nearest-neighbor hopping ($t_2 e^{i\varphi}$) in each hexagon and the central N-sided polygon. In this case, the defective hyperbolic Haldane model can be effectively described by a tight-binding Hamiltonian as

$$H = \sum_{\langle i,j \rangle} t_1 a_i^\dagger a_j + \sum_{\langle\langle i,j \rangle\rangle} t_2 e^{i\varphi} a_i^\dagger a_j + \text{H.c.,} \quad (1)$$

with $a_i^\dagger (a_i)$ being the creation (annihilation) operator at site i. The brackets $< \dots >$ and $<< \dots >>$ indicate summations being restricted within nearest-neighbor and next-nearest-neighbor sites, respectively. In the following, we focus on the case with the polygonal defect being a dodecagon, as shown in Fig. 2(a). Detailed coupling patterns are illustrated in the right insets of Fig. 2(a), where solid lines and dashed arrow lines illustrate the nearest-neighbor and next-nearest-neighbor hoppings, respectively.

To illustrate the topological property of this structure, we first perform a direct diagonalization of Hamiltonian for the defective hyperbolic Haldane lattice with three layers. Other parameters are set as $t_1 = 1$, $t_2 = 0.2$, and $\varphi = 2\pi/3$, respectively. Figure 2(b) presents the numerical result of the associated eigenspectrum. The color map in Fig. 2(b) quantifies the localization degree on outermost boundary sites, which is represented by $V(\varepsilon) = \sum_{i \in 3} |\phi_i(\varepsilon)|^2 / \sum_{i \in L=1,2,3} |\phi_i(\varepsilon)|^2$. $\phi_i(\varepsilon)$ corresponds to the probability amplitude on the ith site with the associated eigenenergy equaling ε. It is clearly shown that boundary states dominate the whole eigenspectrum, and few
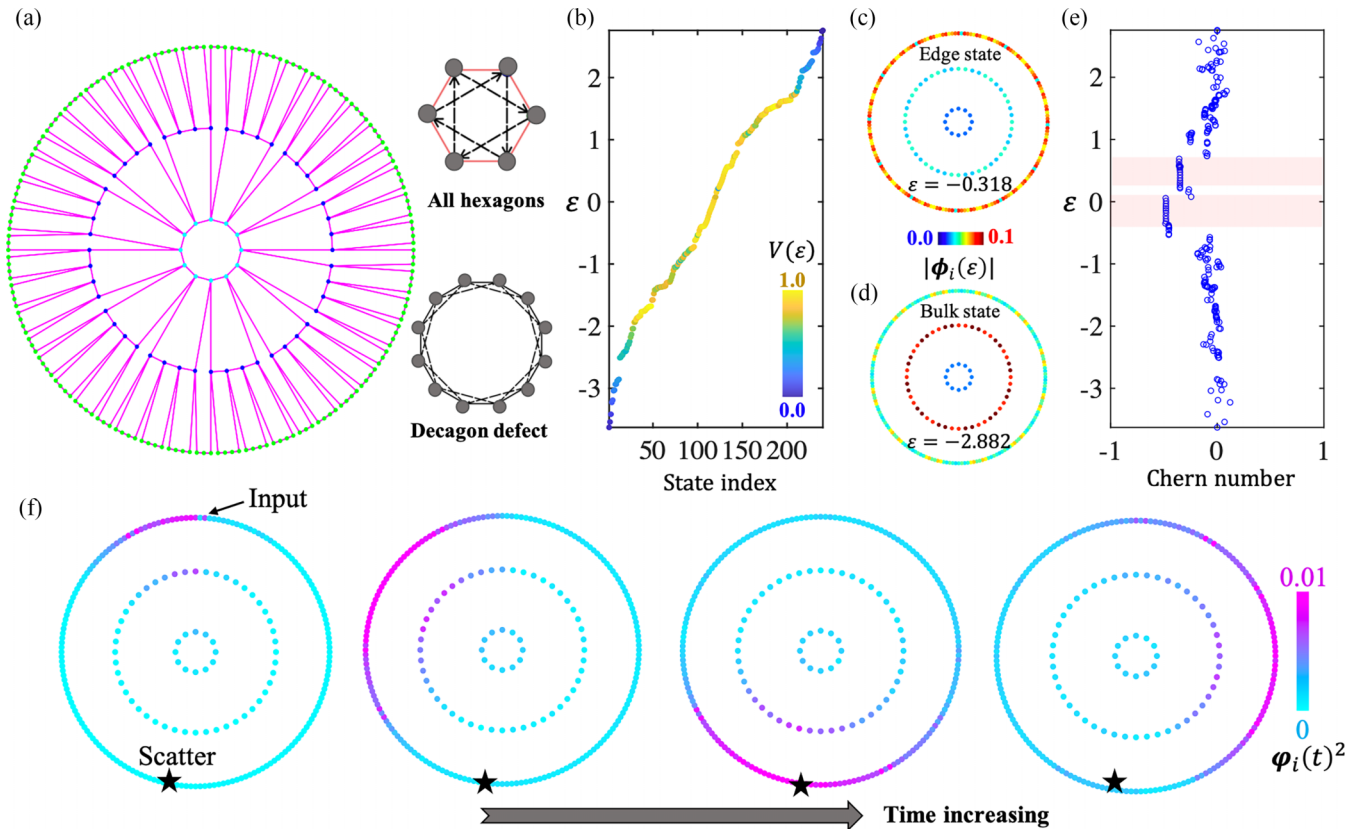
FIG. 2. Numerical results of backscattering-immune topological states in the hyperbolic lattice with a central dodecagon defect. (a) Finite hyperbolic lattice {6,4} with a central dodecagon defect. Right insets plot coupling patterns in hexagons composed of lattice sites from different layers. (b) Calculated eigenspectrum of the system. Color map corresponds to the quantity $V(\varepsilon)$ for the localization degree at the boundary. (c), (d) Profiles of topological-edge state and a bulk state with eigenenergies of -0.318 and -2.882. (e) Calculated real-space Chern number of each eigenmode. (f) Wave-function dynamics of the three-layered hyperbolic lattice with a central dodecagon defect. Four charts present spatial distributions of $|\varphi_i(t)|^2$ at different time.

bulk eigenstates locate at the high-energy region. Figures 2(c) and 2(d) illustrate spatial profiles of a topological-edge state ($\varepsilon = -0.318$) and a bulk state ($\varepsilon = -2.882$), respectively. We can see that the significant boundary and bulk localizations appear for these two eigenmodes. Furthermore, we also calculate the real-space Chern number [39,40] at each eigenenergy, as presented in Fig. 2(e). It is clearly shown that nontrivial platforms of the real-space Chern number appear around the zero energy, where the smaller value (<1) is due to the finite-size effect [35]. In Appendix A, we numerically calculate the real-space Chern number for the defective hyperbolic Haldane model with five layers. We can see that the nontrivial real-space Chern number is converged to $C = -1$ at a nontrivial energy.

In addition, we perform time-domain simulations on the robust propagation of edge states in the defective hyperbolic Haldane model. The excitation signal, which is in the form of $\psi_{\text{in}}(t) = \exp[-(t-30)^2/1225]\sin(\varepsilon_c t)$, is injected into a boundary site (marked by the black arrow). To effectively excite the nontrivial boundary state, we set the excitation energy to $\varepsilon_c = 0$. In addition, a large onsite potential (equaling 5) is also added on a boundary site to act as a scatter (marked by black stars). Four charts in Fig. 2(f) display spatial distributions of wave function at increased time. It is clearly shown that the incident wave pulse unidirectionally propagates on

the boundary of the system, indicating the existence of one-way edge states. To further quantify the backscattering, we calculate the ratio (r) between amplitudes of reflected and transmitted wave packets at two sites, which are clockwise and counterclockwise with respect to the scatter with equal distances. We find that the ratio equals $r = 0.03$, indicating an extremely weak backscattering.

Then, we turn to the two-layer defective hyperbolic Haldane model with the first layer being a 24-sided polygon defect, as shown in Fig. 3(a). We simulate the time-domain dynamics of such a structure by exciting a boundary site [marked by the black arrow in Fig. 3(a)]. The wave packet, which is the same as that of Fig. 2, is used. Figures 3(b) and 3(c) present calculated evolutions of wave function in the defective hyperbolic Haldane model with and without the existence of a boundary scatter (marked by the black star). It is clearly shown that the input signal unidirectionally propagates in the system without the boundary scatter, while different from the above three-layered condition, the significant backscattering (marked by red arrows) appears around the boundary scatter. The ratio between peak amplitudes of reflected and transmitted wave packets at clockwise and counterclockwise sites (marked by blue and red stars), which possess equal distances to the scatter, equals 0.53, manifesting a large backscattering. The disappearance of robust boundary propagation in such
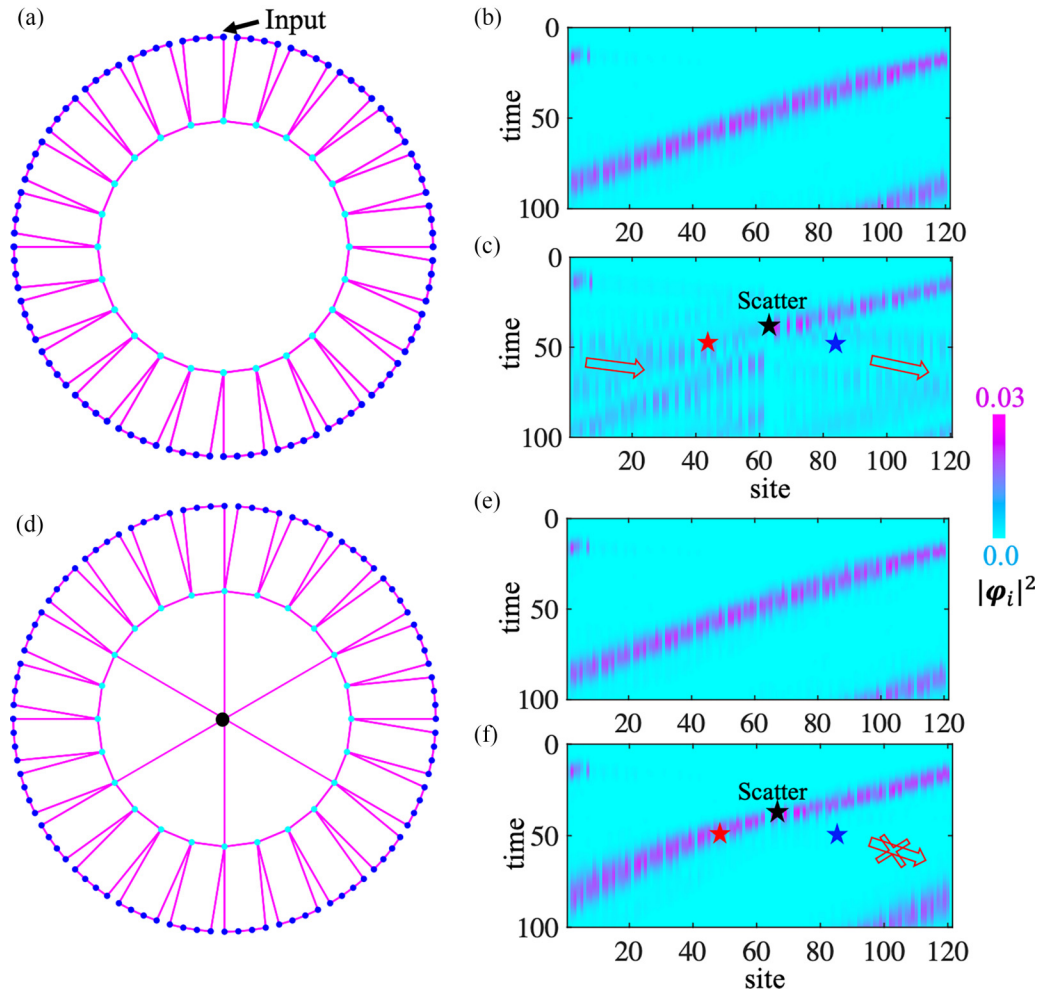
FIG. 3. Numerical results of boundary-dominated one-way topological states in defective hyperbolic Haldane model with a single bulk site. (a) Conceptual drawing of the two-layered defective hyperbolic Haldane model. (b), (c) Time-domain dynamics of wave function in the simplest defective hyperbolic Haldane model with and without the existence of a boundary scatter. (d) Conceptual drawing of the defective hyperbolic Haldane model with a single bulk site. (e), (f) Time-domain dynamics of the defective hyperbolic Haldane model with a single bulk node with and without the existence of a boundary scatter. Black stars mark the scatter. Red and blue stars correspond to clockwise and counterclockwise sites with respect to the scatter with equal distances.

a two-layered defective hyperbolic Haldane model is due to the lack of any bulk site, where all lattice sites belong to the boundary passageway. In this case, there is no other way for the wave function to bypass the boundary scatter, making the significant backscattering appear.

To eliminate the backscattering, it is interesting to ask how many bulk sites are needed to recovery the robust one-way propagation in the defective hyperbolic Haldane model. Here, we subdivide the central face into six hexagons, which effectively adds a third layer and recovers a tiling consisting of only hexagons, as shown in Fig. 3(d). Each hexagon contains nearest-neighbor and next-nearest-neighbor hoppings. Figures 3(e) and 3(f) present numerical results of wave-function dynamics in the system with and without a boundary scatter. We can see that the backscattering around the boundary scatter is nearly zero (highlighted by red arrows), where the ratio between peak amplitudes of reflected and transmitted packets equals to 0.03. This phenomenon clearly manifests that a single bulk site is sufficient to preserve the robust one-way propagation in the defective hyperbolic Haldane model.

In Appendix B, the spatial distributions of wave function at different times are further presented, where the one-way propagations along boundary sites are clearly illustrated. In Appendix C, we further calculate wave-function dynamics in the defective hyperbolic Haldane model with other N-sided polygon defects and a single bulk site. It is found that a single bulk site can still maintain the robustness of edge states in the two-layer defective Haldane model with larger sizes. We note that defective hyperbolic lattices with three or more layers already have many bulk sites without adding the extra one. In this case, the backscattering-immune boundary modes in three (or larger than three)-layered defective Haldane model should be protected by many bulk sites. Moreover, we also calculate the wave-function dynamics by exciting trivial-edge states (see Appendix D), where the robust one-way propagation disappears.

The recovery of the one-way propagation can be understood from the fact that the added single bulk site provides a way for the wave function to bypass the boundary scatter, maintaining the original one-way propagation. In
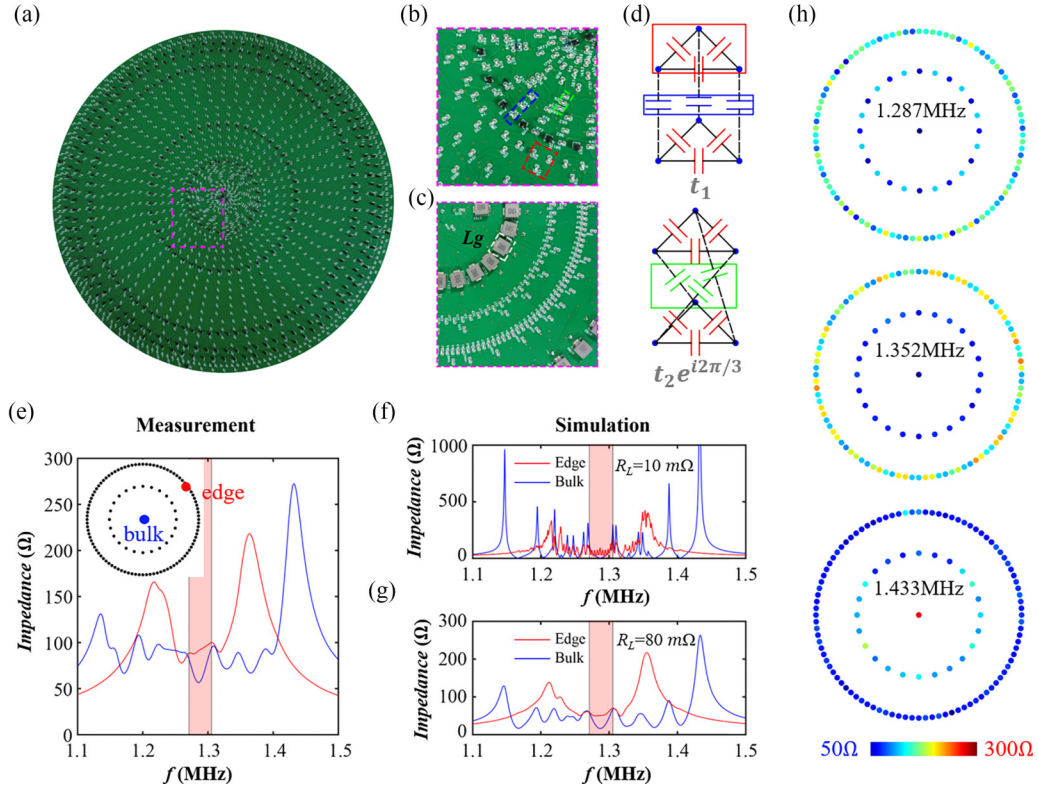
FIG. 4. Observation of boundary-dominated topological states in the defective hyperbolic circuit by impedance spectra. (a) Photograph image of the fabricated hyperbolic circuit. Enlarged views of front and back sides for the circuit are presented in (b) and (c). (d) Equivalent schematic diagrams for realizing real-valued and complex-valued coupling strengths in the designed electric circuit. (e), (f) Measured and simulated impedance responses of bulk (blue lines) and boundary (red lines) nodes. Red region corresponds to the energy range with nontrivial-edge states. (g). Measured impedance distributions at 1.352, 1.287, and 1.433 MHz.

Appendix E, we present numerical results of the eigenspectra and real-space Chern numbers for defective hyperbolic Haldane model with a single bulk node. It is shown that the nontrivial Chern number exists around the zero energy for the boundary state, indicating the existence of topologically protected chiral boundary states. Compared to three-layered site-centered {6,4} lattice, which possesses 72 boundary sites and 5 bulk sites (see Appendix F), our proposed defective hyperbolic model with N-sided polygonal defect possesses a single bulk site and $20N$ boundary sites. Hence, the ratio of boundary sites in the defective hyperbolic lattice is much larger than that of three-layered site-centered {6,4} lattice. In addition, it is worth noting that the single bulk site protected one-way edge states cannot be designed based on the {6,3} Euclidean lattice with polygon defect (see Appendix G for details).

III. OBSERVATION OF BOUNDARY-DOMINATED TOPOLOGICAL STATES IN DEFECTIVE HYPERBOLIC LATTICES BY ELECTRIC CIRCUITS

Motivated by recent experimental breakthroughs in realizing various quantum phases by electric circuit networks [41–58], in the following, we design an electric circuit to observe the boundary-dominated one-way edge states in two-layer defective hyperbolic Haldane model with an extra bulk site. Figure 4(a) illustrates the photograph image of the fabricated circuit sample. Figures 4(b) and 4(c) present enlarged

views of front and back sides for the circuit enclosed by the pink dashed block. Figure 4(d) illustrates the schematic diagram for realizing the real-valued nearest-neighbor hopping and complex-valued next-nearest-neighbor hoppings, respectively. Here, three circuit nodes connected by capacitors C (enclosed by the red dashed block) are considered to form an effective lattice site. To simulate the real-valued nearest-neighbor hopping, three capacitors C_1 (enclosed by the blue dashed block) are used to directly link adjacent nodes without a cross. Differently, for the realization of next-nearest-neighbor hopping rate with complex values, three pairs of adjacent nodes are connected crosswise via three capacitors C_2 (enclosed by the green dashed block). Each node is grounded by an inductor L_g (framed by the white block in the back side) and a conductor C_u. The scatter in the outermost ring is achieved by adding an extra grounding capacitor C_d at three circuit nodes belonging to a single boundary site.

Through the appropriate setting of grounding and connecting, the circuit eigenequation is identical with that of the defective hyperbolic Haldane model. In particular, the probability amplitude is mapped to the voltage pseudospin $V_{\uparrow i, \downarrow i} = V_{i,1} + V_{i,2} e^{\pm i 2\pi/3} + V_{i,3} e^{\mp i 2\pi/3}$, where $V_{i,1}$, $V_{i,2,}$ and $V_{i,3}$ are voltages at three circuit nodes at the ith lattice site. The nearest-neighbor and next-nearest-neighbor hopping strengths equal $t_1 = C_1/C$ and $t_2 = C_2/C$. The complex hopping phase is $\varphi = 2\pi/3$. The eigenenergy (ε) of the lattice model is mapped to the eigenfrequency (f) of the
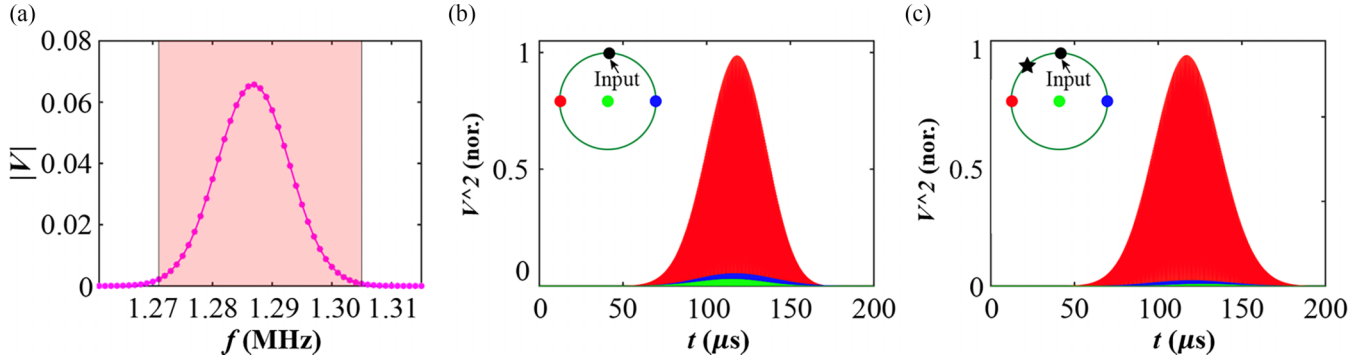
FIG. 5. Observation of the robust propagation of boundary-dominated topological states. (a) Frequency spectrum of injected voltage packet. (b), (c) Measured time tracks of voltage signals at counterclockwise and clockwise boundary nodes and the central bulk node in the circuit without and with a boundary scatter.

circuit with $\varepsilon = f_0^2/f^2 - 3 - (6C_1 + 12C_2 + C_u)/C$, with $f_0 = (2\pi\sqrt{CL_g})^{-1}$. See the detailed derivation of the circuit eigenequation in Appendix H. In the following, we set circuit parameters as $C = 1$ nF, $C_1 = 1$ nF, $C_2 = 0.2$ nF, $C_u = 4$ nF, $L_g = 1\,\mu H$, and $C_P = 5$ nF.

To analyze topological properties of the defective hyperbolic circuit with a single bulk site, we first measure the impedance responses of a bulk node (marked by the blue dot in the inset) and an edge node (marked by the red dot), as shown by blue and red lines in Fig. 4(e). It is well known that the impedance response of a circuit node is related to the local density of states for the mapped lattice model. We can see that there is a minimum of the bulk impedance in the region from 1.25 to 1.29 MHz (marked by the red domain), implying a bulk gap. The larger edge signal in this region results from the excitation of in-gap boundary states. Figures 4(f) and 4(g) plot the simulation results with the effective series resistances of inductance being $R_L = 10$ and 80 mΩ. We can see that the shape of simulated impedance spectra with $R_L = 80$ mΩ is consistent with that of measurements. Little deviations of frequencies and amplitudes for impedance peaks are due to the disorder and dispersion effects for real circuit elements. In particular, the disappearance of edge-impedance peaks in the topological band gap is due to the large loss effect in experiments. In addition, spatial impedance distributions at 1.287, 1.352, and 1.433 MHz are further measured, as shown in Fig. 4(h). It is clearly shown that impedance distributions at these frequencies are matched to spatial profiles of two edge states (with $\varepsilon = -1.547$ and -0.103) and a bulk state ($\varepsilon = -3.06$) shown in Appendix E. In particular, the edge-concentrated impedance profile at 1.287 MHz corresponds to the nontrivial boundary state. Due to the large amplitude of trivial-edge states at the measured edge node, the largest boundary impedance peak corresponds to the excitation of trivial-edge states.

Except for the frequency-dependent impedance spectra, we further measure the voltage dynamics to detect the robust one-way propagation of hyperbolic edge states. Here, the incident voltages at three circuit nodes belonging to a boundary site are in the form of $[V_{i,1}, V_{i,2}, V_{i,3}] = V(t)[1, \exp(i\frac{2\pi}{3}), \exp(-i\frac{2\pi}{3})]$ with $V(t) = V_0\exp[-(t-t_0)^2/t_d^2]\sin(2\pi f_c t)$, $t_0 = 100\,\mu s$,

$t_d = 37\,\mu s$, and $f_c = 1.287$ MHz, respectively. The frequency spectrum of the voltage packet is plotted in Fig. 5(a) and the nontrivial topological band gap is highlighted by the red region. We can see that a large proportion of the frequency spectrum is located in the nontrivial band gap. In this case, the topological-edge state can be dominantly excited by the voltage packet. Red and blue lines in Fig. 5(b) present measured voltage signals at two boundary nodes, which are counterclockwise (marked by the red dot) and clockwise (marked by the blue dot) with respect to the excitation node (marked by black arrows), in the circuit without any boundary scatter. We can see that the counterclockwise circuit node possesses a significant voltage signal, while the voltage signal at the clockwise circuit node is very small. The green line in Fig. 5(b) shows the measured voltage signal at the central bulk node, where the low-voltage signal exists. These experimental results indicate that the input voltage packet can propagate unidirectionally along the boundary of the hyperbolic circuit sample.

Then, we measure the voltage signals in the circuit with a boundary scatter (marked by the black star in the inset). Red and blue lines in Fig. 5(c) display measured voltage signals of two boundary nodes. We can see that the magnitude of the voltage packet at the counterclockwise node is still much larger than that of the clockwise circuit node. The green line in Fig. 5(c) presents the voltage signal of the central bulk node, where the relatively low-voltage signal exists. These measured results indicate the there is no significant backscattering when the voltage signal is passing through the boundary scatter. The voltage dynamics dominated by trivial-edge states is presented in Appendix I, where the robust one-way propagation of voltage pulse disappears.

IV. CONCLUSION

In conclusion, we have studied the backscattering-immune topological states in boundary-dominated hyperbolic lattice with a central polygon defect. We find that the one-way topological states can still exist in the defective hyperbolic Haldane model. Interestingly, we find that only a single bulk site can induce the formation of boundary-dominated one-way propagations in defective hyperbolic lattices. In experiments,
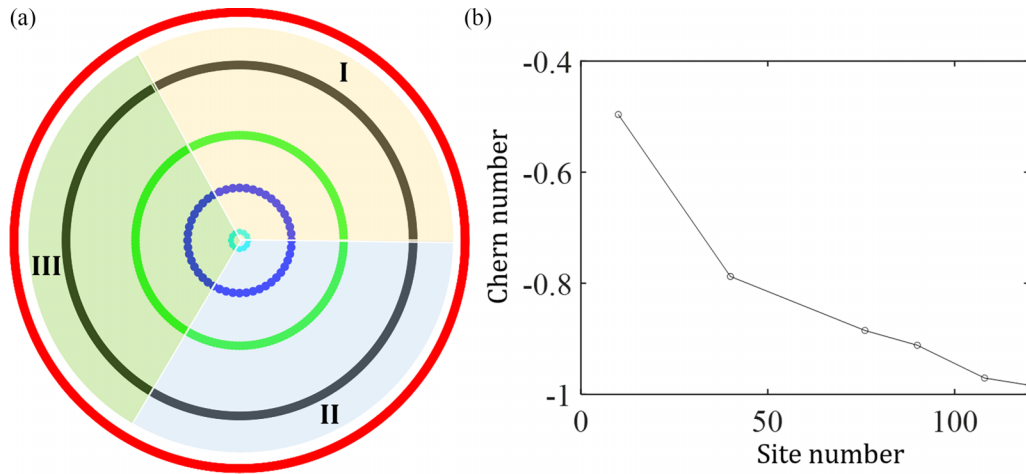
FIG. 6. (a) Illustration of summation regions I, II, and III in the five-layered defective hyperbolic lattice used for calculating the real-space Chern number. (b) Calculated real-space Chern number at $\varepsilon = -0.1424$ with different numbers of lattice sites in the summation region.

we fabricate the defective hyperbolic circuit with a single bulk site to observe the backscattering-immune hyperbolic topological states. The impedance responses clearly illustrate the existence of nontrivial band gaps and in-gap topological boundary states. Furthermore, the one-way propagation of topological-edge states in defective hyperbolic lattices is observed by measuring the dynamics of voltage packets. Our work suggests a useful platform to study topological phases in defective hyperbolic lattices, and may have potential applications in designing high-efficient topological devices with an extremely narrow bulk region.

APPENDIX A: NUMERICAL RESULTS OF REAL-SPACE CHERN NUMBERS FOR LATTICE MODEL WITH A LARGE SIZE

In this appendix, we numerically demonstrate the convergence of the real-space Chern number. The real-space Chern number is defined as $C = 12\pi i \sum_{j \in I} \sum_{k \in II} \sum_{l \in III} (P_{jk}P_{kl}P_{lj} - P_{jl}P_{lk}P_{kj})$, where j, k, and l are site indices in three different regions I, II, and III, as shown in Fig. 6(a). The square of projection operator element $|P_{jk}|^2$ measures the correlation at two sites (i and j) with all eigenstates below the target energy being fully occupied. It is noted that the real-space Chern number does not converge well if the lattice site in the summation region is too close to the boundary of the system or the summation region is too small to contain sufficient numbers of sites. To ensure the convergence of the Chern number to a nontrivial integer, we consider a large defective hyperbolic lattice with five layers, and calculate the real-space Chern number at $\varepsilon = -0.1424$ (within the nontrivial energy region) with different numbers of lattice sites in the summation region, as show in Fig. 6(b). We

can see that as the number of lattice sites in each summation region is increased, the calculated nontrivial Chern number gradually approaches to -1.

APPENDIX B: SPATIAL DISTRIBUTIONS OF ONE-WAY PROPAGATION IN DEFECTIVE HYPERBOLIC HALDANE MODEL WITH A SINGLE BULK SITE

In this appendix, we present detailed spatial profiles of wave-function dynamics in the 24-sided defective hyperbolic Haldane model with a single bulk site. Eight charts in Fig. 7 display the spatial distributions of the wave function with increased time. It is clearly shown that the incident pulse unidirectionally propagates on the boundary of the system, indicating the existence of one-way edge state.

APPENDIX C: ONE-WAY PROPAGATIONS IN DEFECTIVE HALDANE MODELS WITH OTHER TYPES OF N-SIDED REGULAR POLYGON DEFECTS

In this appendix, we demonstrate that single bulk site-triggered one-way edge states also exist in defective Haldane model with other N-sided regular polygon defects. Figure 8(a) presents the two-layered hyperbolic lattice model with a 48-sided polygon defect and a central bulk site. We calculate the wave-function dynamics for the structure, as shown in Fig. 8(b). Figure 8(c) displays spatial distributions of wave function at different time. It is clearly shown that the incident wave function unidirectionally propagates on the boundary with a scatter (marked by black stars), indicating the existence of one-way edge states in the defective hyperbolic Haldane model.

For comparison, we also calculate the wave-function dynamics for the two-layered 48-sided defective hyperbolic lattice model without any central bulk site, as shown in Fig. 9(a). Figures 9(b) and 9(c) display numerical results of wave-function dynamics. It is clearly shown that the significant backscattering appears, as marked by red arrows. We can quantify the backscattering by the ratio between amplitudes of reflected and transmitted packets induced by the scatter. It can be defined by the ratio of peak values of wave packets
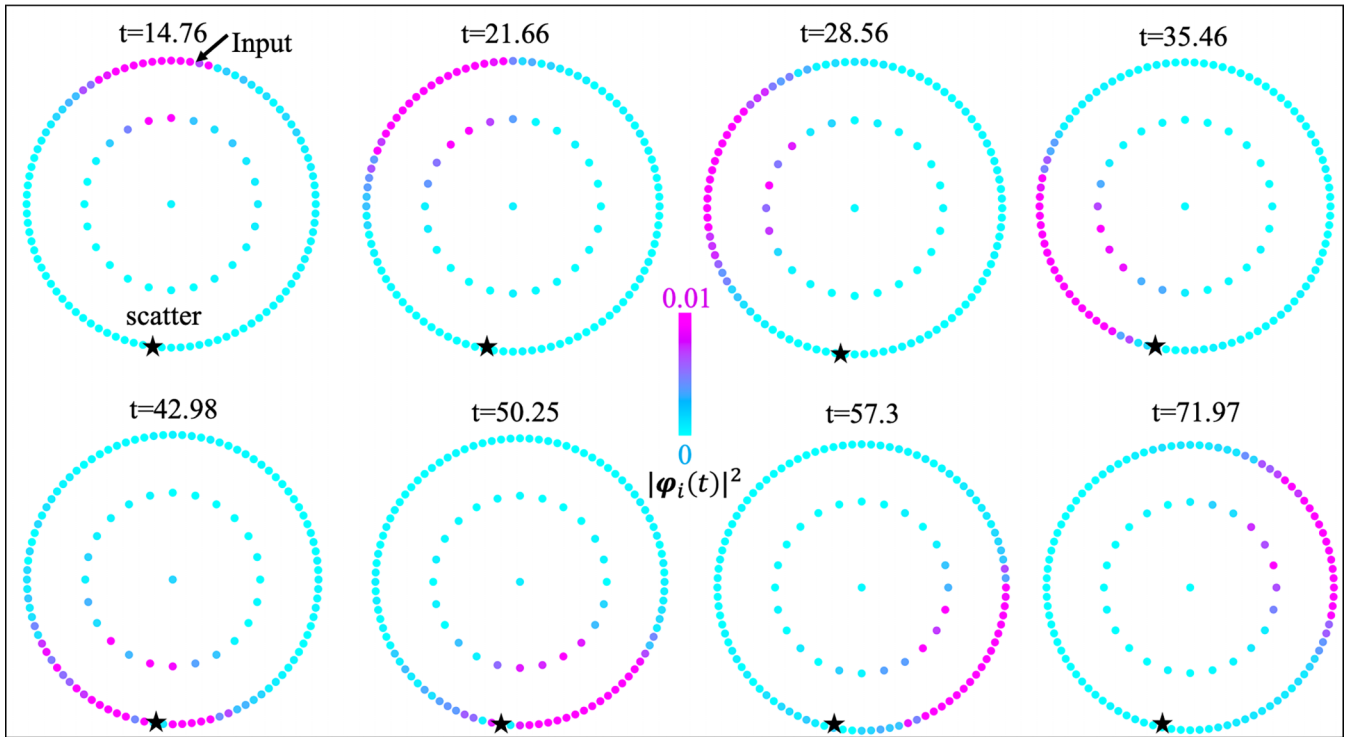
FIG. 7. Spatial distributions of wave function at different time in the defective hyperbolic Haldane model with a single bulk site.

at two sites, which are clockwise and counterclockwise with respect to the boundary scatter with equal distances [marked in Fig. 9(b) by blue and red stars]. We find that $r = 0.07$ ($r = 0.65$) for the 48-sided defective hyperbolic lattice model with (without) a central bulk site, corresponding to the weak

(strong) backscattering. From the above results, we can see that a single bulk site can still remain sufficient to avoid backscattering for larger flakes.

Figures 10(a)–10(d) present numerical results of wave-function dynamics in defective hyperbolic Haldane model
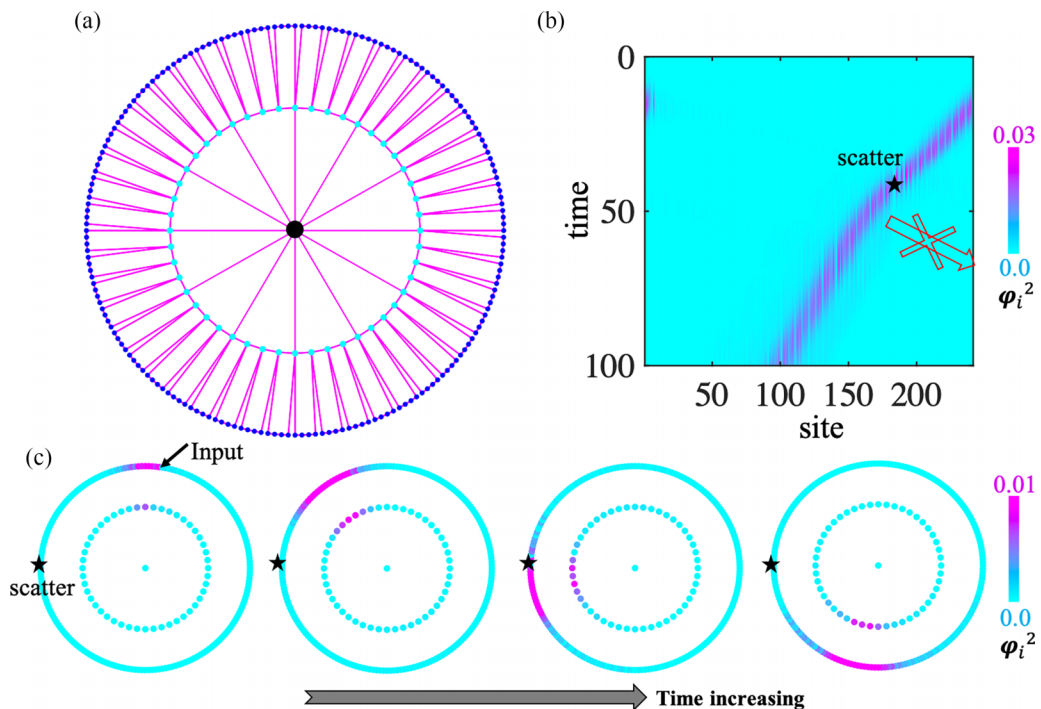

FIG. 8. (a) Two-layered hyperbolic lattice model with a 48-sided polygon defect as well as a central bulk site. (b), (c) Numerical results of wave-function dynamics.
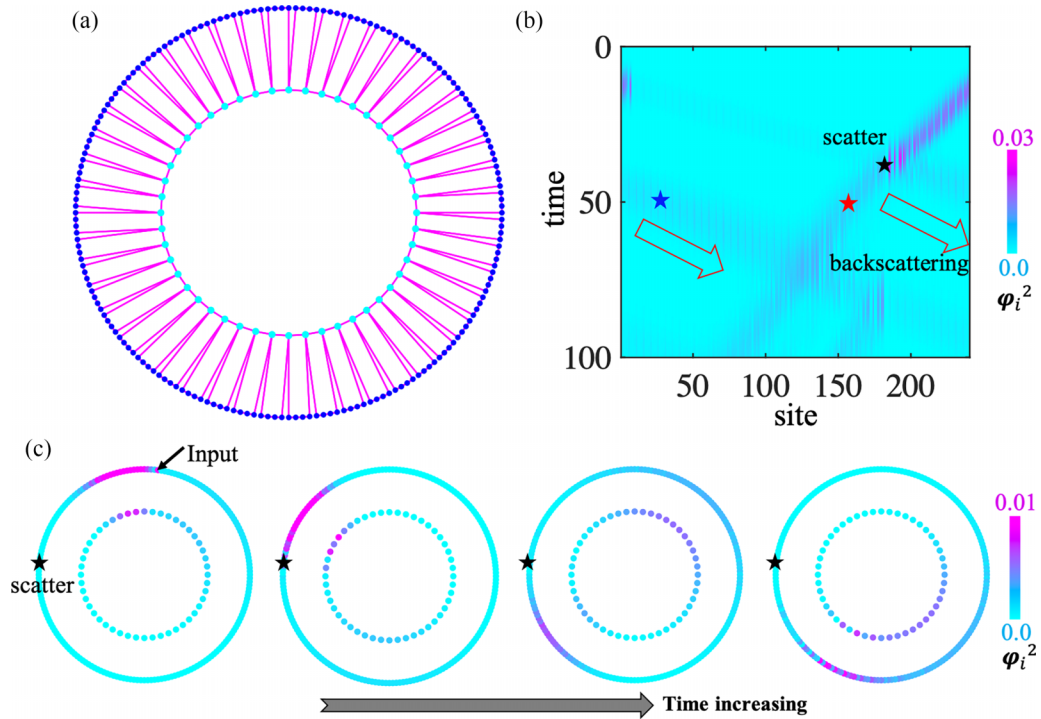
FIG. 9. (a) Two-layered hyperbolic lattice model with a 48-sided polygon defect. (b), (c) Numerical results of wave-function dynamics.

with 48-sided and 12-sided regular polygon defects and a single bulk site. It is clearly shown that the backscattering around the boundary scatter is always zero in each defective hyperbolic Haldane model, manifesting that a single bulk site is sufficient to protect the robust one-way propagation.
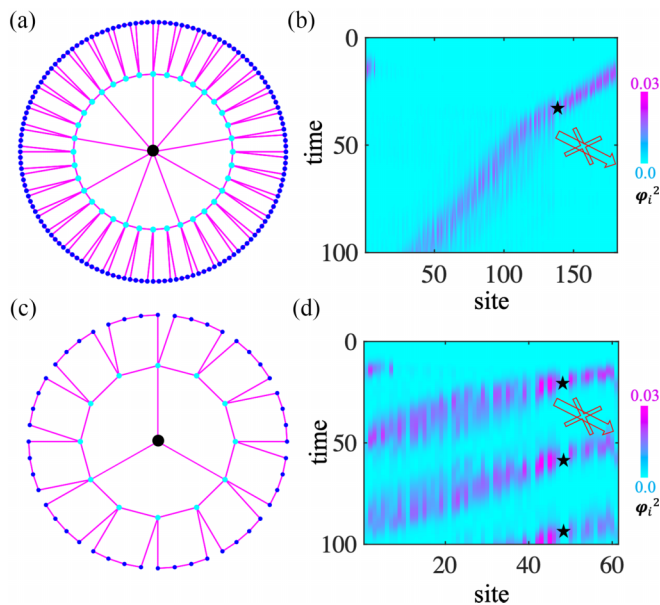

FIG. 10. Wave-function dynamics in different types of defective hyperbolic Haldane model with a single bulk site. (a), (c) Two-layered hyperbolic lattice model with 48-sided and 12-sided polygon defects as well as a central bulk site. (b), (d) Numerical results of wave-function dynamics in defective Haldane model with the 48-sided and 12-sided polygon defects.

APPENDIX D: TRIVIAL-EDGE STATE-DOMINATED WAVE-FUNCTION DYNAMICS IN DEFECTIVE HALDANE MODEL

In this appendix, we investigate the wave-function dynamics dominated by trivial-edge states. We set the input wave-function pules as $\psi_{in}(t) = \exp[-(t-30)^2/1225]\sin(\varepsilon_c t)$, with $\varepsilon_c = -1.547$ (corresponding to the trivial-edge state). Figure 11(a) presents the calculated dynamics of wave function. Figure 11(b) plots spatial profiles of the probability amplitude at different time. We can see that the input signal leaves away from the excited site without chiral behavior, corresponding to the excitation of trivial-edge states.

APPENDIX E: EIGENSPECTRA AND REAL-SPACE CHERN NUMBER FOR TWO-LAYER DEFECTIVE HYPERBOLIC LATTICE WITH AN EXTRA BULK SITE

In this appendix, we clarify the topological property of 24-sided defective hyperbolic Haldane model with a single bulk node. Figure 12(a) presents the numerical result of the
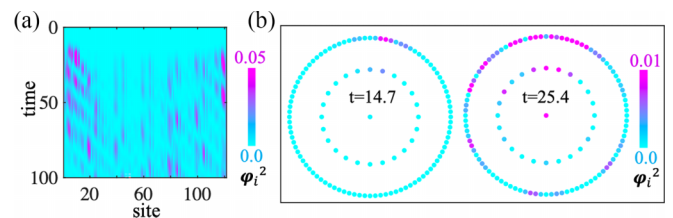

FIG. 11. (a) Calculated wave-function dynamics with the input wave-function packet being $\psi_{in}(t) = \exp[-(t-30)^2/1225]\sin(-1.547t)$. (b) Spatial distributions of $|\varphi_i(t)|^2$ at different time.
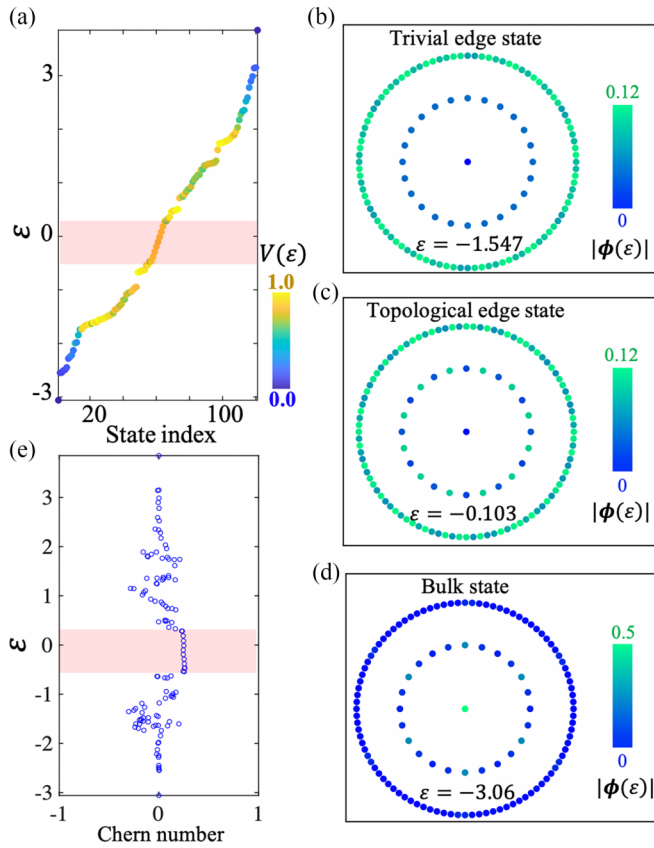
FIG. 12. Numerical results of defective hyperbolic Haldane model with a single bulk node. (a) Calculated eigenspectrum of the system. Color map corresponds to the quantity for the localization degree at the boundary. (b), (c). Profiles of edge and bulk states with eigenenergies of −0.103 and −3.06. (d) Calculated real-space Chern number.

eigenspectrum. The color map quantifies the localization degree on outermost boundary sites. It is clearly shown that hyperbolic boundary states mainly locate on the low-energy region. Figures 12(b)–12(d) illustrate spatial profiles of two edge states ($\varepsilon = -0.103$ and $\varepsilon = -1.547$) and a bulk state ($\varepsilon = -3.06$), respectively. Additionally, we also calculate the real-space Chern number, as presented in Fig. 12(e). We can see that the nontrivial platform around the zero energy exists, as marked by the red region, indicating the existence of topological-edge states.

APPENDIX F: THREE-LAYERED SITE-CENTERED {6,4} LATTICE

In this appendix, we discuss the ratio between boundary and bulk sites in a three-layered site-centered {6,4} lattice. As shown in Fig. 13, dark/light blue and black dots present boundary and bulk sites in the three-layered site-centered {6,4} lattice. We can see that such a structure possesses 72 boundary sites and 5 bulk sites. Our proposed defective hyperbolic model with N-sided polygonal defect only possesses a single bulk site and $20N$ boundary sites. The ratio of

boundary sites in defective hyperbolic lattice is much larger than that of three-layered site-centered {6,4} lattice.

APPENDIX G: {6,3} EUCLIDEAN LATTICE WITH N-SIDED POLYGON DEFECTS

In this appendix, we consider the {6,3} Euclidean lattice with polygon defect. Figure 14(a) presents the {6,3} Euclidean lattice model with a 24-sided polygon defect and a central bulk site. We calculate the eigenspectrum, eigenstates, and the real-space Chern number of the structure, as shown in Figs. 14(b)–14(d). We can see that topological-edge states exist in the region highlighted by red. It is important to note that all of the inner lattice sites work as bulk sites, and only lattice sites at the outermost layer are edge sites. Hence, it is not the single bulk site-protected topological-edge states. Figure 14(e) presents the wave-function dynamics in the system with a boundary scatter (marked by black stars), where the input wave-function pulse is $\psi_{in}(t) = \exp[-(t-30)^2/1225]$. We can see that the one-way propagation exists along lattice sites at the outermost layer, and lattice sites in two inner layers work as bulk sites.

APPENDIX H: DETAILS FOR THE DERIVATION OF THE CIRCUIT EIGENEQUATION

In this appendix, we give a detailed derivation of the circuit eigenequation and the correspondence between the electric circuit and the mapped lattice model. Here, each lattice site possesses three circuit nodes, where the voltage and current at the ith site are written as $V_i = [V_{i,1}, V_{i,2}, V_{i,3}]^T$ and $I_i = [I_{i,1}, I_{i,2}, I_{i,3}]^T$, respectively. In addition, the voltage is in the form of $V_i e^{i\omega t}$. Here, we focus on circuit nodes corresponding to the extra bulk site. Carrying out Kirchhoff's law on three circuit nodes at the extra bulk site, we obtain the following equation:
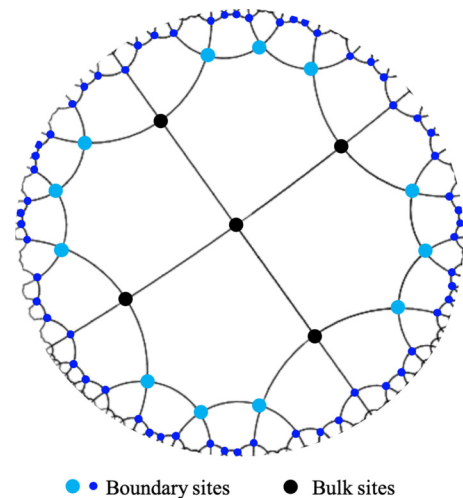

FIG. 13. Three-layered site-centered {6,4} lattice possesses 72 boundary sites (dark/light blue dots) and 5 bulk sites (black dots).
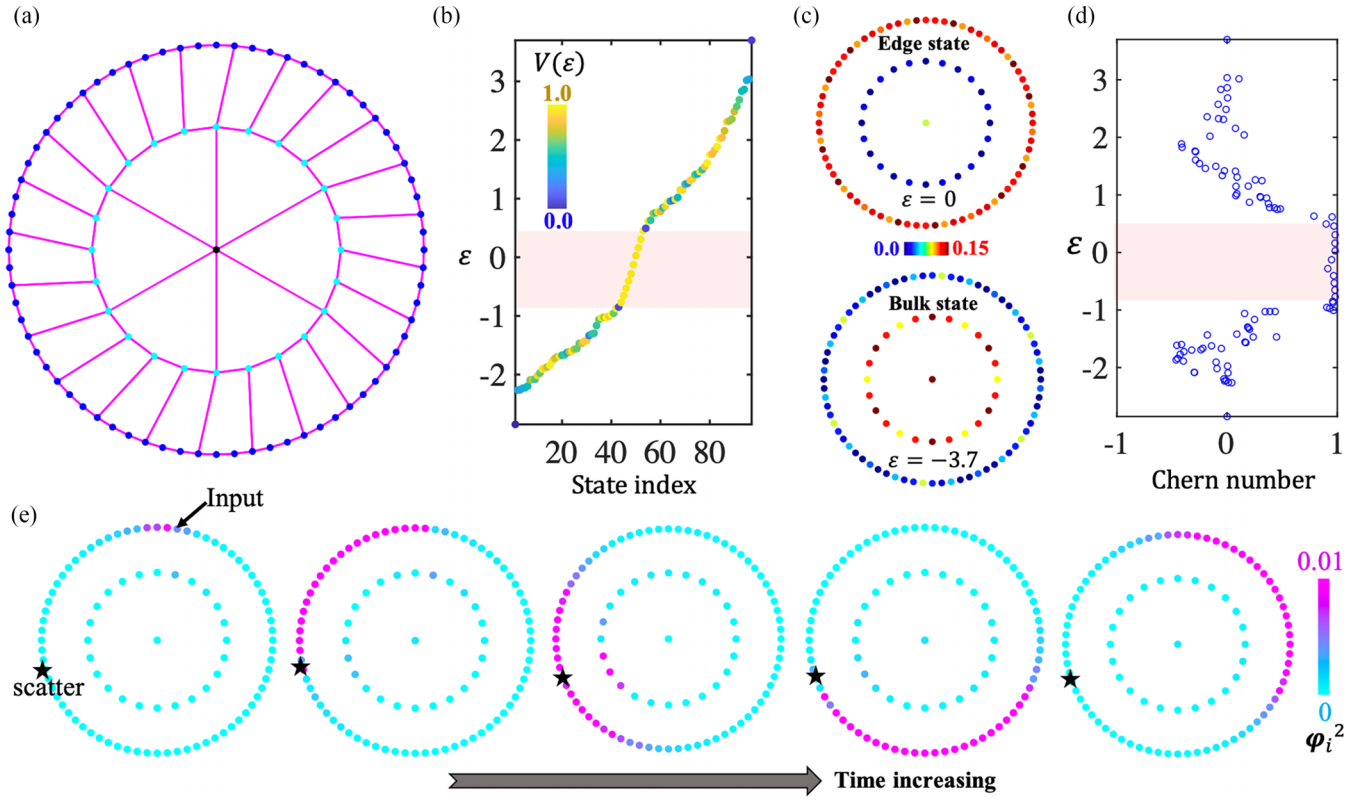
FIG. 14. (a) The {6,3} Euclidean lattice model with a 24-sided polygon defect and a central site. (b)–(d). Calculated eigenspectrum, eigenstates, and real-space Chern numbers of the structure. (e) Wave-function dynamics with a boundary scatter marked by black stars.

$$
\begin{bmatrix} I_{i,1} \\ I_{i,2} \\ I_{i,3} \end{bmatrix} = i\omega^{-1}\left(\omega^2 C \begin{bmatrix} 2 & -1 & -1 \\ -1 & 2 & -1 \\ -1 & -1 & 2 \end{bmatrix}\begin{bmatrix} V_{i,1} \\ V_{i,2} \\ V_{i,3} \end{bmatrix} + \sum_{\langle i,j\rangle} \omega^2 C_1 \begin{bmatrix} V_{i,1} - V_{j,1} \\ V_{i,2} - V_{j,2} \\ V_{i,3} - V_{j,3} \end{bmatrix} + \omega^2 C_u \begin{bmatrix} V_{i,1} \\ V_{i,2} \\ V_{i,3} \end{bmatrix} \sum_{\ll i,j\gg \text{ with } \varphi>0} \omega^2 C_2 \begin{bmatrix} V_{i,1} - V_{j,2} \\ V_{i,2} - V_{j,3} \\ V_{i,3} - V_{j,1} \end{bmatrix} \right.
$$

$$
\left. + \sum_{\ll i,j\gg \text{ with } \varphi<0} \omega^2 C_2 \begin{bmatrix} V_{i,1} - V_{j,3} \\ V_{i,2} - V_{j,1} \\ V_{i,3} - V_{j,2} \end{bmatrix} - \frac{1}{L_g} \begin{bmatrix} V_{i,1} \\ V_{i,2} \\ V_{i,3} \end{bmatrix} \right), \tag{H1}
$$

where C_1 and C_2 are capacitances linking nodes at i to the nearest-neighbor hoppings and next-nearest-neighbor nodes. C is the capacitance used for connecting circuit nodes belonging to a same site. C_u is the grounding capacitance at each site. L_g is the inductor linking circuit nodes to ground. We assume that there is no external current source, so that the current flowing out of the node is zero. In this case, Eq. (H1) becomes

$$
\frac{1}{\omega^2 L_g} \begin{bmatrix} V_{i,1} \\ V_{i,2} \\ V_{i,3} \end{bmatrix} = C\begin{bmatrix} 2 & -1 & -1 \\ -1 & 2 & -1 \\ -1 & -1 & 2 \end{bmatrix}\begin{bmatrix} V_{i,1} \\ V_{i,2} \\ V_{i,3} \end{bmatrix} + (6C_1 + 12C_2 + C_u)\begin{bmatrix} V_{i,1} \\ V_{i,2} \\ V_{i,3} \end{bmatrix} - \sum_{\langle i,j\rangle} C_1 \begin{bmatrix} V_{j,1} \\ V_{j,2} \\ V_{j,3} \end{bmatrix} - \sum_{\ll i,j\gg \text{ with } \varphi>0} C_2 \begin{bmatrix} V_{j,2} \\ V_{j,3} \\ V_{j,1} \end{bmatrix}
$$

$$
- \sum_{\ll i,j\gg \text{ with } \varphi<0} C_2 \begin{bmatrix} V_{j,3} \\ V_{j,1} \\ V_{j,2} \end{bmatrix}. \tag{H2}
$$

Performing the diagonalization of Eq. (H2) with a unitary transformation:

$$
F = \frac{1}{\sqrt{3}}\begin{bmatrix} 1 & 1 & 1 \\ 1 & e^{i2\pi/3} & e^{i4\pi/3} \\ 1 & e^{i4\pi/3} & e^{i8\pi/3} \end{bmatrix}, \tag{H3}
$$

Eq. (H2) becomes

$$\frac{1}{\omega^2 L_g}\begin{bmatrix} V_{i,0} \\ V_{i,\uparrow} \\ V_{i,\downarrow} \end{bmatrix} = C\begin{bmatrix} 0 & 0 & 0 \\ 0 & 3 & 0 \\ 0 & 0 & 3 \end{bmatrix}\begin{bmatrix} V_{i,0} \\ V_{i,\uparrow} \\ V_{i,\downarrow} \end{bmatrix} + (6C_1 + 12C_2 + C_u)\begin{bmatrix} V_{i,0} \\ V_{i,\uparrow} \\ V_{i,\downarrow} \end{bmatrix} - \sum_{<i,j>} C_1\begin{bmatrix} V_{j,0} \\ V_{j,\uparrow} \\ V_{j,\downarrow} \end{bmatrix}$$

$$+ \left(-\Sigma_{-\ll i,j\gg \text{ with } \varphi>0}C_2\begin{bmatrix} 1 & 0 & 0 \\ 0 & e^{(i2\pi)/3} & 0 \\ 0 & 0 & e^{\frac{i2\pi}{3}} \end{bmatrix} - \Sigma_{-\ll i,j\gg \text{ with } \varphi<0}C_2\begin{bmatrix} 1 & 0 & 0 \\ 0 & e^{(i2\pi)/3} & 0 \\ 0 & 0 & e^{\frac{i2\pi}{3}} \end{bmatrix} \right)\begin{bmatrix} V_{j,0} \\ V_{j,\uparrow} \\ V_{j,\downarrow} \end{bmatrix} \quad \text{(H4)}$$

The new basis is $V_{(0,\uparrow,\downarrow),i} = F[V_{i,1}, V_{i,2}, V_{i,3}]^T$, being three decoupled terms. It is noted that two frequency-dependent terms $V_{(\uparrow,\downarrow),i}$ are acting as a pair of voltage pseudospins $V_{\uparrow i} = V_{i,1} + V_{i,2}e^{i2\pi/3} + V_{i,3}e^{-i2\pi/3}$ and $V_{\uparrow i} = V_{i,1} + V_{i,2}e^{-i2\pi/3} + V_{i,3}e^{i2\pi/3}$. Thus, Eq. (H4) on the basis of two pseudospins can be expressed as

$$\frac{1}{\omega^2 L_g C}V_{\uparrow,i} - 3 - (6C_1 + 12C_2 + C_u)/C$$

$$= -\sum_{\langle i,j\rangle} C_1 V_{\uparrow,j} - \sum_{\ll i,j\gg} C_2 e^{\pm i2\pi/3}V_{j,\uparrow}. \quad \text{(H5)}$$

$$\frac{1}{\omega^2 L_g C}V_{\downarrow,i} - 3 - (6C_1 + 12C_2 + C_u)/C$$

$$= -\sum_{\langle i,j\rangle} C_1 V_{j,\downarrow} - \sum_{\ll i,j\gg} C_2 e^{\pm i2\pi/3}V_{j,\downarrow}. \quad \text{(H6)}$$

In this case, we provide the following identification of tight-binding parameters in terms of circuit elements:

$$t_1 = \frac{C_1}{C}, \ t_2 = \frac{C_2}{C}, \ \varphi = \frac{2\pi}{3}, \ \varepsilon = \frac{f_0^2}{f^2}$$

$$- 3 - (6C_1 + 12C_2 + C_u)/C, \ f_0 = \frac{1}{2\pi\sqrt{CL_g}}. \quad \text{(H7)}$$

APPENDIX I: VOLTAGE DYNAMICS WITH EXCITING TRIVIAL-EDGE STATES

In this appendix, we further illustrate the voltage dynamics by exciting the trivial-edge state of the defective hyperbolic circuit with a boundary scatter. Here, parameters of the input voltage packet are set as $t_0 = 100\,\mu s$, $t_d = 37\,\mu s$, and $f_c = 1.352$ MHz, respectively. The associated frequency spectrum is plotted in Fig. 15(a). It is clearly shown that the frequency spectrum locates in the range sustaining trivial-edge states. Red, blue, and green lines in Fig. 15(b) present measured voltage signals of two boundary nodes, which are counterclockwise and clockwise nodes with respect to the excited circuit node, and a central bulk node. We can see that the voltage signal at the circuit node behind the scatter is smaller than others, manifesting the existence of backscattering.
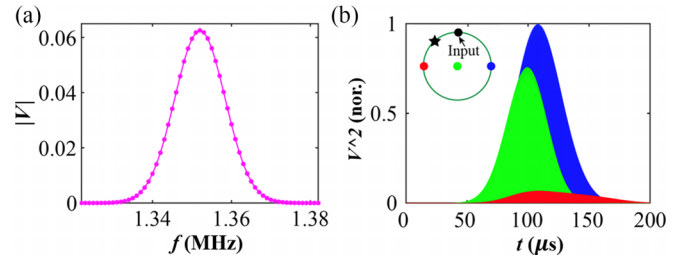

FIG. 15. (a) Frequency spectrum of input voltage packet to excite trivial-edge states. (b) Red, blue, and green lines present measured voltage signals at counterclockwise and clockwise boundary nodes and a central bulk node.

[1] Z.-K. Lin, Q. Wang, Y. Liu, H. Xue, B. Zhang, Y. Chong, and J.-H. Jiang, Topological phenomena at topological defects, arXiv:2208.05082.

[2] A. Rüegg and C. Lin, Bound States of Conical Singularities in Graphene-Based Topological Insulators, Phys. Rev. Lett. **110**, 046401 (2013).

[3] J. C. Y. Teo and T. L. Hughes, Existence of Majorana-Fermion Bound States on Disclinations and the Classification of Topological Crystalline Superconductors in Two Dimensions, Phys. Rev. Lett. **111**, 047006 (2013).

[4] W. A. Benalcazar, J. C. Y. Teo, and T. L. Hughes, Classification of two dimensional topological crystalline superconductors and Majorana bound states at disclinations, Phys. Rev. B **89**, 224503 (2014).

[5] W. A. Benalcazar, T. Li, and T. L. Hughes, Quantization of fractional corner charge in Cn-symmetric higher-order topological crystalline insulators, Phys. Rev. B **99**, 245151 (2019).

[6] T. Li, P. Zhu, W. A. Benalcazar, and T. L. Hughes, Fractional disclination charge in two-dimensional Cn-symmetric topological crystalline insulators, Phys. Rev. B **101**, 115115 (2020).

[7] J. Paulose, B. G.-g. Chen, and V. Vitelli, Topological modes bound to dislocations in mechanical metamaterials, Nat. Phys. **11**, 153 (2015).

[8] C. W. Peterson, T. Li, W. Jiang, T. L. Hughes, and G. Bahl, Trapped fractional charges at bulk defects in topological insulators, Nature (London) **589**, 376 (2021).

[9] Y. Liu, S. Leung, F.-F. Li, Z.-K. Lin, X. Tao, Y. Poo, and J.-H. Jiang, Bulk-disclination correspondence in topological crystalline insulators, Nature (London) **589**, 381 (2021).

[10] Y. Deng, W. A. Benalcazar, Z.-G. Chen, M. Oudich, G. Ma, and Y. Jing, Observation of Degenerate Zero-Energy Topological States at Disclinations in an Acoustic Lattice, Phys. Rev. Lett. **128**, 174301 (2022).

[11] Y. Chen, Y. Yin, Z. H. Zheng, Y. Liu, Z. K. Lin, J. Li, J. H. Jiang, and H. Chen, P-Orbital Disclination States in Non-Euclidean Geometries, Phys. Rev. Lett. **129**, 154301 (2022).

[12] A. K. Nayak, J. Reiner, R. Queiroz, H. Fu, C. Shekhar, B. Yan, C. Felser, N. Avraham, and H. Beidenkopf, Resolving the topological classification of bismuth with topological defects, Sci. Adv. **5**, eaax6996 (2019).

[13] H. Xue, D. Jia, Y. Ge, Y.-j. Guan, Q. Wang, S.-q. Yuan, H.-x. Sun, Y. D. Chong, and B. Zhang, Observation of Dislocation-Induced Topological Modes in a Three-Dimensional Acoustic Topological Insulator, Phys. Rev. Lett. **127**, 214301 (2021).

[14] L. Ye, C. Qiu, M. Xiao, T. Li, J. Du, M. Ke, and Z. Liu, Topological dislocation modes in three-dimensional acoustic topological insulators, Nat. Commun. **13**, 508 (2022).

[15] X.-Q. Sun, P. Zhu, and T. L. Hughes, Geometric Response and Disclination-Induced Skin Effects in Non-Hermitian Systems, Phys. Rev. Lett. **127**, 066401 (2021).

[16] F. Schindler and A. Prem, Dislocation non-Hermitian skin effect, Phys. Rev. B **104**, L161106 (2021).

[17] B. A. Bhargava, I. C. Fulga, J. Van Den Brink, and A. G. Moghaddam, Non-Hermitian skin effect of dislocations and its topological origin, Phys. Rev. B **104**, L241402 (2021).

[18] A. Panigrahi, R. Moessner, and B. Roy, Non-Hermitian dislocation modes: Stability and melting across exceptional points, Phys. Rev. B **106**, L041302 (2022).

[19] W. Magnus, *Noneuclidean Tesselations and Their Groups* (Academic Press, New York, 1974).

[20] A. J. Kollar, M. Fitzpatrick, and A. A. Houck, Hyperbolic lattices in circuit quantum electrodynamics, Nature (London) **571**, 45 (2019).

[21] P. M. Lenggenhager, A. Stegmaier, L. K. Upreti, T. Hofmann, T. Helbig, A. Vollhardt, M. Greiter, C. H. Lee, S. Imhof, H. Brand, T. Kiessling, I. Boettcher, T. Neupert, R. Thomale, and T. Bzdusek, Simulating hyperbolic space on a circuit board, Nat. Commun. **13**, 4373 (2022).

[22] J. Maciejko and S. Rayan, Hyperbolic band theory, Sci. Adv. **7**, eabe9170 (2021).

[23] J. Maciejko and S. Rayan, Automorphic Bloch theorems for hyperbolic lattices, Proc. Natl. Acad. Sci. USA **119**, e2116869119 (2022).

[24] I. Boettcher, A. V. Gorshkov, A. J. Kollár, J. Maciejko, S. Rayan, and R. Thomale, Crystallography of hyperbolic lattices, Phys. Rev. B **105**, 125118 (2022).

[25] I. Boettcher, P. Bienias, R. Belyansky, A. J. Kollár, and A. V. Gorshkov, Quantum simulation of hyperbolic space with circuit quantum electrodynamics: From graphs to geometry, Phys. Rev. A **102**, 032208 (2020).

[26] A. J. Kollar, M. Fitzpatrick, P. Sarnak, and A. A. Houck, Line-graph lattices: Euclidean and non-Euclidean flat bands, and implementations in circuit quantum electrodynamics, Commun. Math. Phys. **376**, 1909 (2020).

[27] A. Chen, H. Brand, T. Helbig, T. Hofmann, S. Imhof, A. Fritzsche, T. Kieling, A. Stegmaier, L. K. Upreti, and T. Neupert, Hyperbolic matter in electrical circuits with tunable complex phases, Nat Commun **14**, 622 (2023).

[28] K. Ikeda, S. Aoki, and Y. Matsuki, Hyperbolic band theory under magnetic field and Dirac cones on a higher genus surface, J. Phys.: Condens. Matter **33**, 485602 (2021).

[29] P. Bienias, I. Boettcher, R. Belyansky, A. J. Kollar, and A. V. Gorshkov, Circuit Quantum Electrodynamics in Hyperbolic Space: From Photon Bound States to Frustrated Spin Models, Phys. Rev. Lett. **128**, 013601 (2022).

[30] N. Cheng, F. Serafin, J. McInerney, Z. Rocklin, K. Sun, and X. Mao, Band Theory and Boundary Modes of High-Dimensional Representations of Infinite Hyperbolic Lattices, Phys. Rev. Lett. **129**, 088002 (2022).

[31] A. Attar and I. Boettcher, Selberg trace formula in hyperbolic band theory, Phys. Rev. E **106**, 034114 (2022).

[32] X. Zhu, J. Guo, N. P. Breuckmann, H. Guo, and S. Feng, Quantum phase transitions of interacting bosons on hyperbolic lattices, J. Phys.: Condens. Matter **33**, 335602 (2021).

[33] S. Yu, X. Piao, and N. Park, Topological Hyperbolic Lattices, Phys. Rev. Lett. **125**, 053901 (2020).

[34] A. Stegmaier, L. K. Upreti, R. Thomale, and I. Boettcher, Universality of Hofstadter Butterflies on Hyperbolic Lattices, Phys. Rev. Lett. **128**, 166402 (2022).

[35] W. Zhang, H. Yuan, N. Sun, H. Sun, and X. Zhang, Observation of novel topological states in hyperbolic lattices, Nat. Commun. **13**, 2937 (2022).

[36] Z.-R. Liu, C.-B. Hua, T. Peng, and B. Zhou, Chern insulator in a hyperbolic lattice, Phys. Rev. B **105**, 245301 (2022).

[37] D. M. Urwyler, P. M. Lenggenhager, I. Boettcher, R. Thomale, T. Neupert, and T. Bzdusek, Hyperbolic Topological Band Insulators, Phys. Rev. Lett. **129**, 246402 (2022).

[38] W. Zhang, F. Di, X. Zheng, H. Sun, and X. Zhang, Hyperbolic band topology with non-trivial second Chern numbers, Nat. Commun. **14**, 1083 (2023).

[39] A. Kitaev, Anyons in an exactly solved model and beyond, Ann. Phys. **321**, 2 (2006).

[40] N. P. Mitchell, L. M. Nash, D. Hexner, A. M. Turner, and W. T. M. Irvine, Amorphous topological insulators constructed from random point sets, Nat. Phys. **14**, 380 (2018).

[41] J. Ningyuan, C. Owens, A. Sommer, D. Schuster, and J. Simon, Time- and Site-Resolved Dynamics in a Topological Circuit, Phys. Rev. X **5**, 021031 (2015).

[42] V. V. Albert, L. I. Glazman, and L. Jiang, Topological Properties of Linear Circuit Lattices, Phys. Rev. Lett. **114**, 173902 (2015).

[43] C. H. Lee, S. Imhof, C. Berger, F. Bayer, J. Brehm, L. W. Molenkamp, T. Kiessling, and R. Thomale, Topolectrical circuits, Commun. Phys. **1**, 39 (2018).

[44] S. Imhof, C. Berger, F. Bayer, J. Brehm, L. W. Molenkamp, T. Kiessling, F. Schindler, C. H. Lee, M. Greiter, and T. Neupert, Topolectrical-circuit realization of topological corner modes, Nat. Phys. **14**, 925 (2018).

[45] T. Helbig, T. Hofmann, C. H. Lee, R. Thomale, S. Imhof, L. W. Molenkamp, and T. Kiessling, Band structure engineering and reconstruction in electric circuit networks, Phys. Rev. B **99**, 161114(R) (2019).

[46] Y. Wang, H. M. Price, B. Zhang, and Y. D. Chong, Circuit implementation of a four-dimensional topological insulator, Nat. Commun. **11**, 2356 (2020).

[47] N. A. Olekhno, E. I. Kretov, A. A. Stepanenko, P. A. Ivanova, V. V. Yaroshenko, E. M. Puhtina, D. S. Filonov, B. Cappello, L. Matekovits, and M. A. Gorlach, Topological edge states of interacting photon pairs emulated in a topolectrical circuit, Nat. Commun. **11**, 1436 (2020).

[48] W. Zhang, D. Zou, Q. Pei, W. He, J. Bao, H. Sun, and X. Zhang, Experimental Observation of Higher-Order Topological Anderson Insulators, Phys. Rev. Lett. **126**, 146802 (2021).

[49] M. Di Ventra, Y. V. Pershin, and C.-C. Chien, Custodial Chiral Symmetry in a Su-Schrieffer-Heeger Electrical Circuit with Memory, Phys. Rev. Lett. **128**, 097701 (2022).

[50] D. Zou, T. Chen, W. He, J. Bao, C. H. Lee, H. Sun, and X. Zhang, Observation of hybrid higher-order skin-topological effect in non-Hermitian topolectrical circuits, Nat. Commun. **12**, 7201 (2021).

[51] S. S. Yamada, T. Li, M. Lin, C. W. Peterson, T. L. Hughes, and G. Bahl, Bound states at partial dislocation defects in multipole higher-order topological insulators, Nat. Commun. **13**, 2035 (2022).

[52] A. Stegmaier, S. Imhof, T. Helbig, T. Hoefmann, C. H. Lee, M. Kremer, A. Fritzsche, T. Feichtner, S. Klembt, S. Hofling, I. Boettcher, I. C. Fulga, L. Ma, O. G. Schmidt, M. Greiter, T. Kiessling, A. Szameit, and R. Thomale, Topological Defect Engineering and PT Symmetry in Non-Hermitian Electrical Circuits, Phys. Rev. Lett. **126**, 215302 (2021).

[53] W. Zhang, F. Di, H. Yuan, H. Wang, X. Zheng, L. He, H. Sun, and X. Zhang, Observation of non-Hermitian aggregation

effects induced by strong interactions, Phys. Rev. B **105**, 195131 (2022).

[54] S. Liu, R. Shao, S. Ma, L. Zhang, O. You, H. Wu, Y. J. Xiang, T. J. Cui, and S. Zhang, Non-Hermitian skin effect in a non-Hermitian electrical circuit, Research **2021**, 5608038 (2021).

[55] W. Zhang, H. Yuan, H. Wang, F. Di, N. Sun, X. Zheng, H. Sun, and X. Zhang, Observation of Bloch oscillations dominated by effective anyonic particle statistics, Nat. Commun. **13**, 2392 (2022).

[56] M. Kremer, I. Petrides, E. Meyer, M. Heinrich, O. Zilberberg, and A. Szameit, A square-root topological insulator with non-quantized indices realized with photonic Aharonov-Bohm cages, Nat. Commun. **11**, 907 (2020).

[57] W. Zhang, D. Zou, J. Bao, W. He, Q. Pei, H. Sun, and X. Zhang, Topolectrical-circuit realization of a four-dimensional hexadecapole insulator, Phys. Rev. B **102**, 100102(R) 2020).

[58] L. Song, H. Yang, Y. Cao, and P. Yan, Realization of the square-root higher-order topological insulator in electric circuits, Nano Lett. **20**, 7566 (2020).